Distortions of the Hubble diagram: Line-of-sight signatures of local galaxy clusters

Jenny G. Sorce, Roya Mohayaee, Nabila Aghanim, Klaus Dolag, Nicola Malavasi

A&A, 687, A85 (2024)
https://doi.org/10.1051/0004-6361/202349073

Astronomy & Astrophysics

Distortions of the Hubble diagram: Line-of-sight signatures of local galaxy clusters

Jenny G. Sorce[1,2,3], Roya Mohayaee[4,5], Nabila Aghanim[2], Klaus Dolag[6,7], and Nicola Malavasi[8]

[1] Univ. Lille, CNRS, Centrale Lille, UMR 9189 CRIStAL, 59000 Lille, France
e-mail: jenny.sorce@univ-lille.fr
[2] Université Paris-Saclay, CNRS, Institut d'Astrophysique Spatiale, 91405 Orsay, France
[3] Leibniz-Institut für Astrophysik, An der Sternwarte 16, 14482 Potsdam, Germany
[4] CNRS, UPMC, Institut d'Astrophysique de Paris, 98 bis Bld Arago, Paris, France
[5] Rudolf Peierls Centre for Theoretical Physics, University of Oxford, Parks Road, Oxford OX1 3PU, UK
[6] University Observatory Munich, Scheinerstr. 1, 81679 München, Germany
[7] Max-Planck Institut für Astrophysik, Karl-Schwarzschild Str. 1, 85741 Garching, Germany
[8] Max Planck Institute for Extraterrestrial Physics, Giessenbachstrasse 1, 85748 Garching, Germany

Received 22 December 2023 / Accepted 16 April 2024

ABSTRACT

The Universe expansion rate is modulated around local inhomogeneities due to their gravitational potential. Velocity waves are then observed around galaxy clusters in the Hubble diagram. This paper studies them in a ∼738 Mpc-wide, 2048^3-particle cosmological simulation of our cosmic environment (a.k.a. CLONE: Constrained LOcal & Nesting Environment Simulation). For the first time, the simulation shows that velocity waves that arise in the lines of sight of the most massive dark matter halos agree with those observed in local galaxy velocity catalogs in the lines of sight of Coma and several other local (Abell) clusters. For the best-constrained clusters such as Virgo and Centaurus – that is, those closest to us – secondary waves caused by galaxy groups, further into the non-linear regime, also stand out. This match was not utterly expected given that before being evolved into a fully non-linear $z = 0$ state, assuming ΛCDM, CLONE initial conditions are constrained solely with linear theory, the power spectrum, and highly uncertain and sparse local peculiar velocities. Additionally, Gaussian fits to velocity wave envelopes show that wave properties are tightly tangled with cluster masses. This link is complex, though, and involves the environment and formation history of the clusters. A proposed metric, measuring the distance between the observed and several re-centred simulated lines of sight, waves included, is shown to be capable of providing a tight mass range estimate for massive local clusters. Using machine learning techniques to grasp more thoroughly the complex wave-mass relation, velocity waves could in the near future be used to provide additional and independent mass estimates from galaxy dynamics within large cluster radii.

Key words. methods: statistical – techniques: radial velocities – catalogs – galaxies: clusters: general – galaxies: kinematics and dynamics

1. Introduction

As the largest gravitationally bound structures in the Universe, galaxy clusters bear imprints of the cosmic growth visible through the distribution and motion of galaxies in their surrounding environment (see Kravtsov & Borgani 2012, for a review and references therein). They constitute, therefore, powerful complementary probes to supernovae and baryon acoustic oscillations in testing theories explaining the origin of cosmic acceleration (see Weinberg et al. 2013, for a review). Relations between halo masses and observables (optical galaxy richness, the Sunyaev-Zel'dovich effect, and X-ray luminosity) must however be calibrated beforehand to study the evolution of the cluster mass function. Our capacity to discriminate among cosmological models is thus tightly linked to the accuracy of cluster mass estimates. However, most of the cluster matter content is not directly visible, making their mass estimates a particularly challenging task (see for a review Pratt et al. 2019; Planck Collaboration XXIV 2016).

With future imaging surveys to come (LSST, Burke 2006; *Euclid*, Peacock 2008; WFIRST, Green et al. 2012), stacked weak lensing measurements will certainly provide the best cluster mass estimates; in other words, with the 1% accuracy required (Mandelbaum et al. 2006) but limited to small radii around clusters. Independent virial mass estimators (Heisler et al. 1985), hydrostatic estimators for galaxy populations (Carlberg et al. 1997), or velocity caustics (boundaries between galaxies bound to and escaping from the cluster potential, Diaferio 1999) constitute complementary tools once calibrated. Their calibration suffers, though, from the influence of baryonic physics and galaxy bias on velocity fields and dispersion profiles. Perhaps velocity caustics are less prone to such systematics (Diaferio 1999), explaining their recent increased popularity. Galaxy clusters can indeed be seen as disrupters of the expansion, creating a velocity wave first mentioned by Tonry & Davis (1981) as a triple-value region[1] whose properties (mostly height and width) depend on the cluster mass. Combined with infall models (Tully & Shaya 1984;

[1] Such an appellation derives directly from the fact that in a distorted Hubble diagram, galaxies at three distinct distances, d, share a similar velocity value whereas in an unperturbed diagram, these galaxy velocities would differ precisely because of the expansion proportional to $H_0 \times d$.

Mohayaee & Tully 2005), velocities of galaxies in the infall zones thus constitute good mass proxies for galaxy clusters shown to be in good agreement with virial mass estimates (Tully 2015). They have been used in different studies to retrieve the total amount of dark matter in groups and clusters as well as to detect groups (e.g. Karachentsev et al. 2013; Karachentsev & Nasonova 2013). They have also permitted the identification of interlopers in galaxy clusters and of wrongly assigned distances to galaxies (Sanchis et al. 2004; Mamon et al. 2010). Moreover, Zu et al. (2014) showed that the wave shape is a nice complementary probe: for instance, f(R) modified gravity models enhance the wave height (infall velocity) and broaden its width (velocity dispersion). This translates into a higher mass when considering a Λcold dark matter (CDM) framework. Subsequently, it would lead to cosmological tensions between S_8 values measured with the cosmic microwave background and with the galaxy cluster counts. Furthermore, velocity waves probe a cluster mass within radii larger than those reached with weak lensing. Subsequently, combined together, stacked weak lensing and velocity wave mass measurements hold tighter constraints on dark energy than each of them separately. Indeed, velocity waves are signatures of a tug of war between gravity and dark energy. Differences between these two independent mass estimates, one dynamic and one static, permit measuring the gravitational slip between the Newtonian and curvature potentials. This constitutes a nice test of gravity.

Given future galaxy redshift and large spectroscopic follow-up surveys (with *Euclid*, Peacock 2008; 4MOST, de Jong et al. 2012; MOONS, Cirasuolo et al. 2014) of imaging ones, studying galaxy infall kinematics to derive better cluster dynamic mass estimates is surely the next priority. Cosmological simulations constitute critical tools to test, understand, and eventually calibrate this mass estimate method applied to galaxy cluster observations. Ideally these simulations must be constrained simulations[2] to properly set the zero point of the method. Namely, simulations must be designed to ensure that the simulated and observed waves match in every aspect, but if the theoretical model somewhere fails and not because of, for instance, different formation histories and/or environments. We are now able to produce such simulations that are valid down to the cluster scale, including the formation history of the clusters (e.g. Sorce et al. 2016a, 2019, 2021; Sorce 2018). These simulations are faithful reproductions of our local environment, including its clusters such as Virgo, Coma, Centaurus, Perseus, and several Abell clusters. Unlike previous analytical work using cluster-centric frames to compare simulated and observed velocity waves of similar mass clusters (Peirani & de Freitas Pacheco 2006), these simulations allow us to directly compare simulated and observed full lines of sight (as seen from the Milky Way) that include the clusters.

This paper thus starts with the first comparison between line-of-sight velocity waves due to several observed local clusters and their counterparts from a Constrained LOcal & Nesting Environment (CLONE) simulation built within a ΛCDM framework. First, we present the numerical CLONE used in this study. Next, we compare the observed and simulated lines of sight that host velocity waves. To facilitate the comparisons, the background expansion was subtracted. Wave envelopes were, then, fitted to study relations between wave properties and cluster masses in a ΛCDM cosmology. Before concluding, a metric, measuring the distance between the observed and re-centred simulated lines of sight, waves included, is proposed in order to deduce a mass range estimate of the clusters they host.

[2] The initial conditions of such simulations stem from observational constraints applied to the density and velocity fields.

2. The CLONE simulation

Constrained simulations are designed to match the local large-scale structure around the Local Group. Several techniques have been developed to build the initial conditions of such simulations (e.g. Gottlöber et al. 2010; Kitaura 2013; Jasche & Wandelt 2013) with density, velocity, or both constraints. Here, we used the technique whose details (algorithms and steps) are described in Sorce et al. (2016a), Sorce (2018). Local observational data used to constrain the initial conditions were distances of galaxies and groups (Tully et al. 2013; Sorce & Tempel 2017) converted to peculiar velocities (Sorce et al. 2016b; Sorce & Tempel 2018) that were bias-minimised (Sorce 2015). We showed that constrained simulations obtained with this particular technique (CLONE; Sorce et al. 2021) are, to our knowledge, currently the sole replicas of the local large-scale structure that include the largest local clusters using only galaxy peculiar velocities as constraints. Namely, the cosmic variance of replicas (a constrained simulation set) is effectively reduced within a 200 Mpc radius centred on the Local Group down to the cluster scale – in other words, 3–4 Mpc (Sorce et al. 2016a) – with respect to that of a random simulation set. Galaxy clusters (such as Virgo, Centaurus, and Coma) have masses in agreement with observational estimates (Sorce 2018; Hernández-Martínez et al. 2024). Several ensuing studies focused in particular on the galaxy clusters. These studies confirmed the necessity of using CLONES to get a high-fidelity Virgo-like cluster. Additionally, they confirmed observationally based formation scenarios of the latter (Olchanski & Sorce 2018; Sorce et al. 2019, 2021). They also highlighted projection effects on its hydrostatic mass, in particular due to a group on the same line of sight as Virgo (Lebeau et al. 2024b), and dynamic state effects on its splashback radius measurement (Lebeau et al. 2024a). Another work looked at the cosmic web surrounding the Coma cluster and recovered the observed filaments (Malavasi et al. 2023). One of the latest studies determined the peculiarities of the distribution of the local clusters, in terms of mass and position, with respect to that of clusters in random patches (Dolag et al. 2023).

To actually probe a large range of velocities in the infall zones, the CLONE for the present study needs to have a sufficient resolution to simulate, with a hundred particles at $z = 0$, halos of intermediate mass ($\sim 10^{11}$–$10^{12}\,M_\odot$). Moreover, Peirani (2010) showed that a dark-matter-only simulation is sufficient for velocity wave studies. They indeed found similar results when adding baryons. They found no major difference regarding cluster outskirt dynamics on these scales. The constrained initial conditions of the CLONE thus contain 2048^3 dark matter particles in a ∼738 Mpc co-moving box (particle mass $\sim 10^9\,M_\odot$). It ran on more than 10 000 cores from $z = 120$ to $z = 0$ in the *Planck* cosmology framework ($\Omega_m = 0.307$; $\Omega_\Lambda = 0.693$; $H_0 = 67.77\,\mathrm{km\,s^{-1}\,Mpc^{-1}}$ and $\sigma_8 = 0.829$, Planck Collaboration XVI 2014) using the adaptive mesh refinement RAMSES code (Teyssier 2002). The mesh is dynamically (de-)refined from levels 11 to 18 according to a pseudo-Lagrangian criterion; namely, when the cell contains more (less) than eight dark matter particles. The initial coarse grid is thus adaptively refined up to a best-achieved spatial resolution of ∼2.8 kpc, roughly constant in proper length (a new level is added at expansion factors $a = 0.1, 0.2, 0.4, 0.8$ up to level 18 after $a = 0.8$).

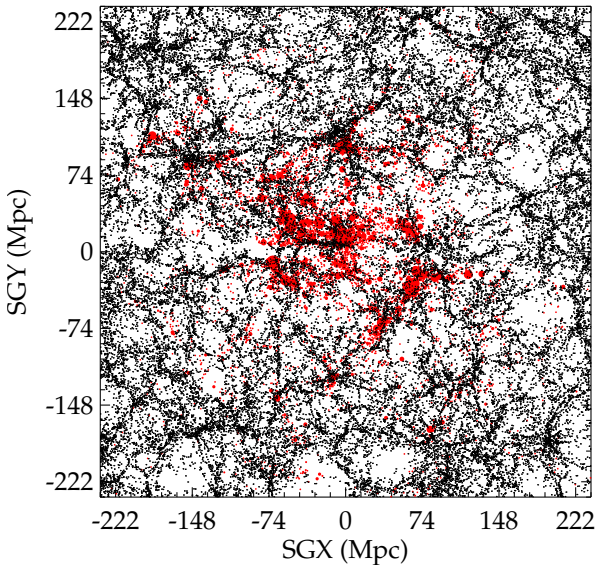

Fig. 1. ~30 Mpc-thick XY supergalactic slice of the CLONE. Black dots stand for the dark matter halos (subhalos are excluded for clarity). Red dots are galaxies and groups from the grouped 2MRS catalog for comparison purposes only (compressed Fingers-of-God from Tempel et al. 2018). Indeed, only a small fraction of local galaxy observational redshifts have been used to derive peculiar velocities that were used as constraints (about ~2.5% of the 2MRS catalog). Red dot sizes are proportional to the richness of the groups. Observed groups (large red dots) are on top of simulated dark matter halos (black dots). No large red dot appears to be overlaid on the middle of a simulated void.

Using the halo finder, described in Aubert et al. (2004) and Tweed et al. (2009), modified to work with 2048^3 ($>2^{31}$) particles, dark matter halos and subhalos are detected in real space with the local maxima of dark matter particle density field. Their edge is defined as the point where the overdensity of dark matter mass drops below 80 times the background density. We further applied a lower threshold of a minimum of 100 dark matter particles. Figure 1 shows the ~30 Mpc-thick XY supergalactic slice of the CLONE. Black (red) dots stand for the dark matter halos (galaxies from the grouped 2MASS Galaxy Redshift Catalog, Huchra et al. 2012; Tempel et al. 2018). Red dot sizes are proportional to the richness of the groups. 2MASS Galaxy Redshift (2MRS) catalog galaxies were used solely for comparison purposes. The 2MRS is indeed far more complete than the peculiar velocity catalog used to constrain the simulation (~2.5% of the redshift catalog is used to derive the peculiar velocity). In fact, it shows the constraining power of the peculiar velocities that are correlated on large scales. Namely, the simulation is also constrained in regions where no peculiar velocity measurements were available and used as constraints. It confirms that peculiar velocity catalogs fed into our technique, to reconstruct or constrain the local density and velocity fields, do not need to be complete (Sorce et al. 2017).

3. Velocity wave

3.1. In simulated data

Positioning a synthetic observer at the simulation box centre, we derived radial peculiar velocities for all the dark matter halos and subhalos in the $z = 0$ catalog. We then drew lines of sight in the direction of each dark matter halo more massive than $5 \times 10^{14}\,M_\odot$. All the (sub)halos within 10 Mpc of the line of sight

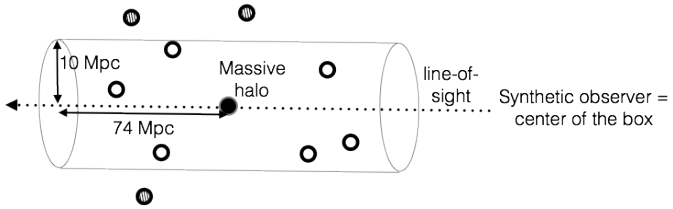

Fig. 2. Schema of the cylinder used to select (sub)halos whose radial peculiar velocities, derived as a function of the synthetic observer at the simulated box centre, were used to study the velocity wave arisen from the massive halo in its centre. While open circles stand for selected halos, dashed circles represent excluded ones.

and within 74 Mpc along the line of sight from a given massive dark matter halo (with the centre and edge of the box as the upper limits) were selected to plot the latter corresponding velocity wave. Namely, as is shown in Fig. 2, radial peculiar velocities, with respect to the synthetic observer, of (sub)halos within a cylinder at a maximum of 148 Mpc long and 20 Mpc wide were used to visualise the velocity wave caused by the massive dark matter halo in the cylinder centre. Because the simulation is constrained to reproduce the local Universe, we chose not to use the periodic boundary conditions when analysing the simulation. It will indeed not be representative of local structures. A 10 Mpc-radius cylinder corresponds to about three times the virial radius of the massive clusters under study here ($M > 5 \times 10^{14}\,M_\odot$). Since the goal is to study the link between velocity wave properties and cluster masses, exact masses cannot be used to define the cylinder shape. Finally, such large volumes permit probing the infall region around the massive halos. A cylinder shape is preferable to a cone shape to get an unbiased wave signal. A cone would indeed result in a distorted signal as it would probe a larger and larger region around a massive halo with distance.

3.2. In observational data

Observational data were taken from the raw second and third catalogs of the Cosmicflows project (Tully et al. 2013, 2016). The second catalog, containing ~8000 galaxies with a mean distance of ~90 Mpc, served as the basis to build the constraint catalog of ~5000 bias-minimised radial peculiar velocities of galaxies and groups with a mean distance of ~60 Mpc. By contrast, the third catalog contains ~17 000 galaxies with a mean distance of ~120 Mpc. The third catalog was not used to constrain our CLONE initial conditions, and thus partly constitutes an independent dataset for consistency checks. More precisely, it serves the two-fold goal of extending the number of observational data points to be compared with the simulation and highlighting the constraining power of peculiar velocities. The latter can indeed permit the recovery of structures that are not directly probed and that are at the limit of the non-linear threshold. In the sense that there is no direct measurement in a given region but, because the latter influences the velocities of other regions (large-scale correlations), it can still be reconstructed.

Uncertainties on distances and radial peculiar velocities in these catalogs depend on the distance indicator used to derive the distance moduli. Error bar sizes need to be limited to see clearly velocity waves. Thus, to be able to compare observed and simulated waves, only galaxies with uncertainties on distance moduli smaller than 0.2 dex were retained. There remained 338 and 424 galaxies, respectively, from the second and third catalogs, with a mean distance of ~50 Mpc. These galaxies were mostly hosts of

supernovae, especially those farthest from us (the distance indicator has a small uncertainty, even as the distance increases).

To derive the radial peculiar velocities of these galaxies, we used both galaxy distance moduli (μ) and observational redshifts ($z_{\rm obs}$), following Davis & Scrimgeour (2014). We added supergalactic longitude and latitude coordinates to derive galaxy Cartesian supergalactic coordinates. A cosmological model was then required to determine peculiar velocities. While we used ΛCDM, as Cosmicflows catalog zero points are calibrated through a long process on WMAP (rather than *Planck*) values ($\Omega_m = 0.27$, $\Omega_\Lambda = 0.73$, $H_0 = 74\,{\rm km\,s^{-1}\,Mpc^{-1}}$, Tully et al. 2013, 2016), we had to use the same parameter values. We indeed showed that when applying the bias minimisation technique to the peculiar velocity catalog of constraints, we reduce the dependence on ΛCDM cosmological parameter values (Sorce & Tempel 2017). However, in order to be able to probe the whole velocity wave for the comparisons, we had to use the raw catalog; that is, with neither galaxy grouping nor bias minimisation. Consequently, if we were to take *Planck* values to derive galaxy peculiar velocities, the WMAP calibration would translate into a residual Hubble flow visible in the background-expansion-subtracted Hubble diagram. Subsequently, using WMAP values for the observations:

– Luminosity distances, $d_{\rm lum}$, were derived from distance modulus measurements, μ, obtained via distance indicators:

$$\mu = 5\log_{10}(d_{\rm lum}\ ({\rm Mpc})) + 25. \quad (1)$$

– Cosmological redshifts, $z_{\rm cos}$, were then obtained through the equation (Weinberg 1972)

$$d_{\rm lum} = (1 + z_{\rm cos}) \int_0^{z_{\rm cos}} \frac{c{\rm d}z}{H_0 \sqrt{(1+z)^3\Omega_m + \Omega_\Lambda}}. \quad (2)$$

– Galaxy radial peculiar velocities, $v_{\rm pec}$, were finally estimated by using the observational $z_{\rm obs}$ and cosmological $z_{\rm cos}$ redshifts with the following formula (Weinberg 1972):

$$v_{\rm pec} = c\frac{z_{\rm obs} - z_{\rm cos}}{1 + z_{\rm cos}}, \quad (3)$$

where $v_{\rm pec}$ always refers to the radial peculiar velocity in this paper and c is the speed of light.

3.3. Simulated versus observed data

Assuming that the synthetic observer is at the box centre and the simulated volume is oriented similarly to the local volume, observed and simulated positions and lines of sight can be matched. We could only compare velocity waves born from local galaxy clusters for which infalling galaxy peculiar velocities, with uncertainties on corresponding distance moduli smaller than 0.2 dex, were available in the observed cluster surroundings. We thus selected these clusters. For each simulated massive dark matter halo, the quickest way was then to search for the closest observed galaxy in the above-selected samples, with a radial peculiar velocity greater than $1000\,{\rm km\,s^{-1}}$ ($\sim 2\sigma$ above the average). This is indeed a signature that it most probably has an observed cluster with a mass of at least a few $10^{14}\,M_\odot$ as a neighbour. Whenever a simulated massive dark matter halo is within the 2σ uncertainty of the observed galaxy distance, we selected all the observed galaxies in the cylinder corresponding to the line of sight. In every case, there is indeed a massive observed cluster in the vicinity of the galaxies. More to the point, given the supergalactic coordinates of the observed clusters and those of the simulated ones in the box, they match.

Figure 3 superimposes observed and simulated lines of sight that include velocity waves born from the two closest, most massive local clusters. Observational data are of sufficient quality in the infall regions to warrant adequate comparisons. From left to right, galaxy clusters (dark matter halos) lie at an increasing distance from us (the synthetic observer). The names of the clusters are indicated at the top of each panel. Filled black and grey circles stand for simulated (sub)halos, while filled light blue and orange squares and diamonds represent observed galaxies. Because the simulation was run with $H_0 = 67.77\,{\rm km\,s^{-1}\,Mpc^{-1}}$, filled dark blue and red squares and diamonds are observed galaxies at positions re-scaled with this latter value. Position differences are within about the 1σ uncertainty on the distance. Arrows indicate the position of the most massive halos in the lines of sight of interest.

In the top panels, the Hubble diagrams are distorted by the presence of massive halos. Their corresponding velocity wave or triple-value region signatures show up. The bottom panels, with the Hubble flow subtracted, equally confirm the waves. The simulated velocity waves of the two massive dark matter halos emerge in the peculiar velocity of (sub)halos plotted as a function of their distance from the synthetic observer diagrams. There is a qualitative match with the observational data points, all the more so since only sparse peculiar velocities of today's field galaxies and groups were used to constrain the linear initial density and velocity fields, at the positions of the latter progenitors, using solely linear theory and a power spectrum, assuming a given cosmology. The full non-linear theory was then used to evolve these initial conditions from the initial redshift down to $z = 0$ within a ΛCDM framework.

The signatures of Virgo West and the group around NGC4709, which are, respectively, beyond Virgo and Centaurus in the lines of sight, can also be identified as secondary waves. These smaller waves follow the highest ones representing the main clusters in both the observational and the simulated lines of sight. There exists a visual agreement between the observed line-of-sight dynamical states of Virgo and Centaurus and those reproduced by CLONE. Comparisons with another constrained simulation, called SIBELIUS (McAlpine et al. 2022), shown in the appendix, reveal that an agreement at this level of detail between the full observed and constrained simulated lines of sight was not utterly expected.

To quantify the agreement between simulated and observed lines of sight, we used a two-dimensional (2D) Kolmogorov-Smirnov (KS) statistic test applied to the simulated and observed galaxy velocity and position samples. The 2D KS is an extension of the non-parametric KS test to 2D probability distributions (Peacock 1983; Fasano & Franceschini 1987). Like the KS test, it permits comparing samples by quantifying the distance between their distributions. Table 1 gives the 2D KS statistic or the highest distance between the cumulative distribution functions of the observed and simulated lines of sight that contain the velocity waves. A single 2D KS statistic value has no particular meaning but several together permit ordering the simulated lines of sight from those that match their observational counterpart most closely to those that match it the least (smallest to largest values). Virgo's line of sight happens to be slightly better reproduced by the simulation than Centaurus' one. 2D KS statistic values barely differ when considering all the subhalos or galaxies within a 10 Mpc radius or solely those within a 2.5 Mpc radius of the line of sight. The agreement is comparable whether using galaxies from the second catalog (CF2) of the Cosmicflows project or those of the third one. Given that the third catalog has more points and smaller uncertainties, it is

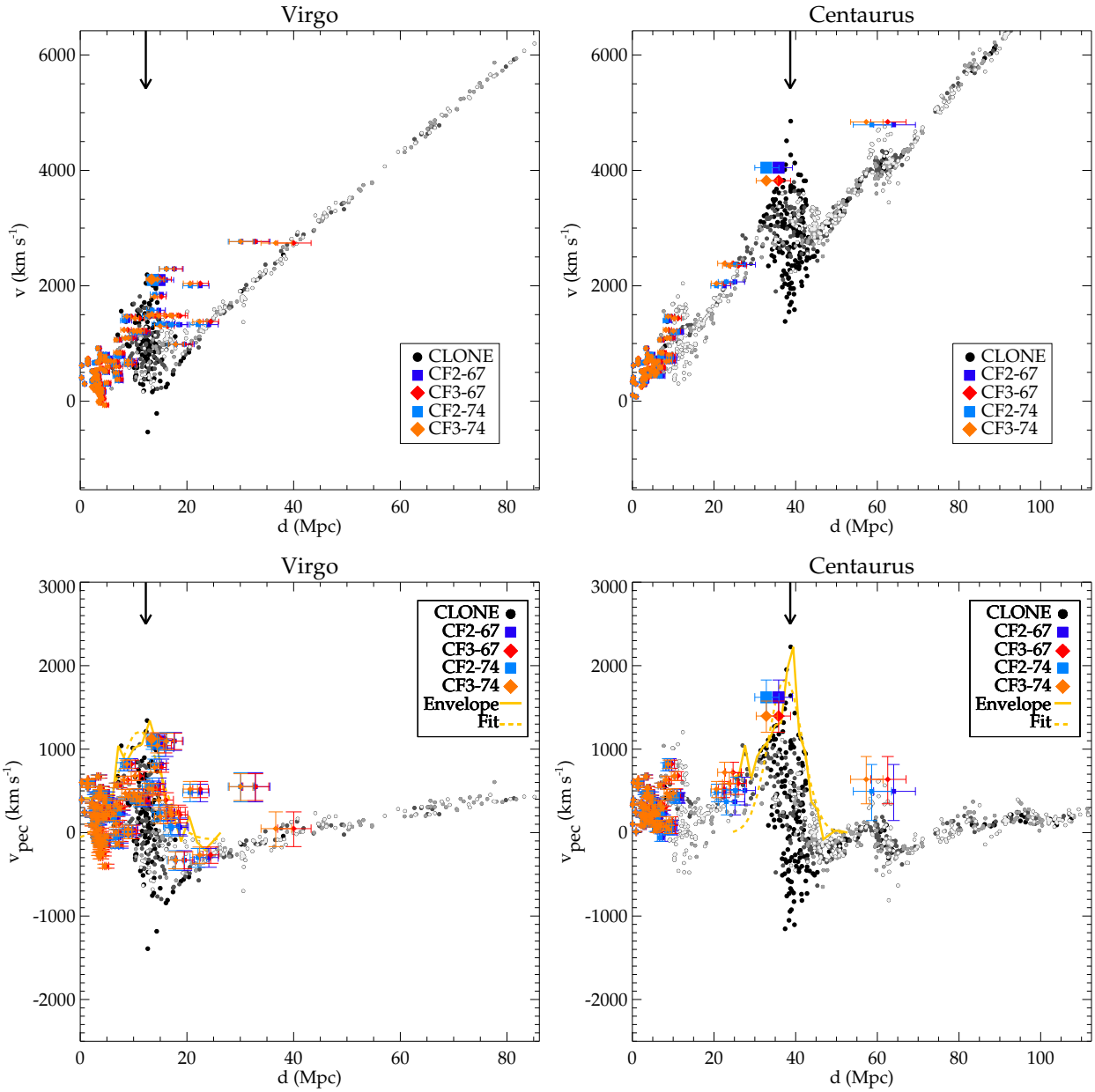

Fig. 3. Radial velocities of simulated dark matter (sub)halos (black and grey) and observed galaxies (orange, blue, and red) as a function of the distance from the synthetic observer and us, respectively. Error bars stand for uncertainties on observational distance and velocity estimates. Orange and light blue (red and dark blue) filled squares and diamonds show observed galaxies, assuming $H_0 = 74$ (67.77) km s^{-1} Mpc^{-1} for scaling positions. CF2 (CF3) corresponds to the second (third) catalog of the Cosmicflows project. Larger symbols are used for galaxies with a peculiar velocity higher than 1000 km s^{-1}, identified as the closest to the simulated massive halos, assuming the synthetic observer at the box centre and the same supergalactic coordinate system and orientation as the local Universe. The arrow indicates the position of the massive dark matter halo in the simulation. Names of corresponding observed clusters are given at the top of each panel. Velocity waves stand out in the different lines of sight and there is a nice agreement with observational data points for those two best-constrained clusters, the closest to us. Top: Hubble diagram. Bottom: Hubble flow subtracted in the observations ($H_0 = 74$ km s^{-1} Mpc^{-1}; see the text for explanation on the zero point choice of the observational catalog) and not added in the simulation. The solid and dashed yellow lines are, respectively, the simulated positive-half velocity wave envelope and its Gaussian-plus-continuum fit. The colour scale filling the black circles stands for their distance from the line of sight. From black to light grey, objects are less than 2.5, 5, 7.5, and 10 Mpc away from the line of sight. The dark matter halo virial masses in the simulation are $M = 9.8 \times 10^{14}\ M_\odot$ and $M = 9.0 \times 10^{14}\ M_\odot$ for the Virgo and Centaurus cluster counterparts, respectively.

encouraging that the values are comparable. Indeed, if the third catalog is closer to the true signal (smaller uncertainties) than the second catalog, the simulation, whose goal is to reproduce the true signal, should tend toward the former. The 2D KS statistic test cannot, however, take into account observational uncertainties. Finally, 2D KS statistic values do not differ when using $H_0 = 67.77$ rather than 74 km s^{-1} Mpc^{-1}.

The 2D KS statistic test cannot take into account the real distance of galaxies. Schematically, it compares only a combination of the four cumulative distributions of galaxies along the lines of sight obtained using four directions for counting (smallest to largest distances on the y axis and vice versa, in which there is no distance to the observer, and smallest to largest distances on the x axis – in that case velocities because they are centred on zero –

Table 1. KS statistic or highest distance between the cumulative distribution functions of the observed and simulated lines of sight.

Cluster	CLONE/CF2		CLONE/CF3	
Cylinder radius	10 Mpc	2.5 Mpc	10 Mpc	2.5 Mpc
Virgo	0.73	0.73	0.73	0.71
Centaurus	0.81	0.89	0.86	0.94
Abell 569	0.83	0.99	0.50	0.56
Coma	0.84	0.96	0.84	0.96
Abell 85	1.0	1.0	1.0	1.0
Abell 2256	1.0	1.0	1.0	1.0
PGC 765572	0.63	0.63	0.99	0.92
PGC 999654	1.0	1.0	1.0	1.0
PGC 340526	0.75	0.75	1.0	1.0
PGC 46604	1.0	1.0	1.0	1.0

Notes. The latter include the velocity waves.

Table 2. ζ metric in km s^{-1}.

Cluster	CLONE/CF2		CLONE/CF3		Random/CF3
Cylinder radius	10 Mpc	2.5 Mpc	10 Mpc	2.5 Mpc	2.5 Mpc
Virgo	163	304	157	304	11 200
Centaurus	173	348	171	343	11 221
Abell 569	294	1998	155	1392	7272
Coma	275	722	485	820	6276
Abell 85	386	727	718	1082	2392
Abell 2256	1453	1454	1491	1491	2882
PGC 765572	1137	1137	1066	1067	2447
PGC 999654	747	747	685	685	2769
PGC 340526	875	907	704	736	1728
PGC 46604	1341	1341	1341	1341	2800

Notes. It measures the difference between the simulated and observed lines of sight. The higher ζ is, the more different the lines of sight are. The last column gives the average ζ value when comparing 1100 random simulated lines of sight and the observed ones. The random lines of sight were selected to contain at least one halo more massive than $10^{14}\,M_\odot$; see the text for a detailed explanation.

and vice versa). Consequently, we also defined our own ζ metric to compare simulated and observed lines of sight as follows:

$$\zeta = \frac{1}{n}\sum_{i=1}^{n} \min\{\sqrt{[v_{\rm obs}[i] - v_{\rm sim}]^2 + [(d_{\rm obs}[i] - d_{\rm sim}) \times H_0]^2}\}, \quad (4)$$

where n is the number of observed galaxies in the line of sight. v_X are the galaxy or subhalo observed and simulated peculiar velocities and d_X are their distances.

Table 2 gives the values of ζ for the different lines of sight. ζ values are only slightly modified by a few percent when changing the H_0 value. The numbers are slightly in favour of 67.77 km s^{-1} Mpc^{-1} though. Consequently, those for 74 km s Mpc^{-1} are reported in the table and should be seen as an upper limit. Like for the 2D KS statistic values, ζ values permit ordering the simulated lines of sight (including waves) that are the best reproduction of the observed ones to those that reproduce them the less. Our ζ metric seems appropriate as it results in conclusions similar to those obtained with the 2D KS statistic. However, unlike the 2D KS statistic, the ζ metric is sensitive to the real distance of the cluster. It includes differences due to both a difference in height and a shift in position along the entire line of sight. A test consists of drawing random lines of sight that each include one of the 1100 most massive halos (minimum mass $\sim 10^{14}\,M_\odot$) in the simulation. There are then compared to the observed lines of sight that include the local clusters given in Table 2. The resulting average ζ values are given in the last column of Table 2. Values are at least about two to ten times larger than when comparing observed lines of sight and their replica in CLONE. The ζ metric still does not take into account uncertainties. A different metric would be needed to include asymmetric uncertainties on velocities and distances that are lognormal distributed.

In the rest of the paper, we work solely with the background expansion subtracted since it does not affect our conclusion and ease the comparisons, studies, and analyses.

Although, by construction, the simulation matches best the local large-scale structure in the inner part, where most of the constraints are, Fig. 4 shows an additional four massive halos that are more distant. These halos are still in agreement with observational clusters that are further away. Tables 1 and 2 confirm the visual impression. The values obtained for both metrics also show the metric limitations and confirm their complementarity. On the one hand, the ζ metric is more robust to small samples than the 2D KS statistic. For example, Abell 569 has a smaller observational sample in the second catalog of the Cosmicflows project than in the third one. The ζ values when comparing both observational samples to the simulated one differ by only a few percent. The 2D KS statistic values grandly differ. One the other hand, the 2D KS statistic is more robust to observational uncertainties. Given their uncertainties, the peculiar velocity values of galaxies in Coma and Abell 85's surroundings are compatible with both the second and third catalogs of the Cosmicflows project. They are higher though in the third catalog. This results in higher ζ metric values when comparing lines of sight from this third catalog to the simulated one rather than those from the second catalog to the simulated one. It is not completely unexpected that the simulated lines of sight more closely match those from the second catalog than the third one at a fixed number of data points and similar uncertainties. Indeed, the second catalog is the starting point to build the constrained initial conditions. More precisely, peculiar velocity values of groups and field galaxies in this area at $z = 0$ were used to estimate their progenitors' position and velocity through the reconstruction of the displacement or velocity fields. These progenitors' positions and velocities were then used to constrain the initial conditions. The initial conditions were then evolved. There is, finally, a (non-linear) relation between the final wave and the initial constraints. There is, however, no convolution as non-field galaxy peculiar velocities were not used to directly and individually constrain the initial conditions that were, moreover, evolved down to $z = 0$.

Since observed galaxies with low distance uncertainties are usually not exactly on the line of sight of the massive clusters, their velocity constitutes a lower limit for the mass estimate of the observed clusters. Indeed, galaxies perfectly aligned with the observer and the cluster would have the highest possible velocity but such galaxies are difficult to distinguish from those belonging to the cluster. Consequently, for Virgo, Centaurus, and Abell 569, the maximum peculiar velocity in the simulation is slightly higher than that in the observations. It confirms that the simulated clusters have reached the low mass limit set by the observations. Moreover, the difference between the observed and simulated wave maxima is small enough that masses are within the same mass range according to the least action modeling

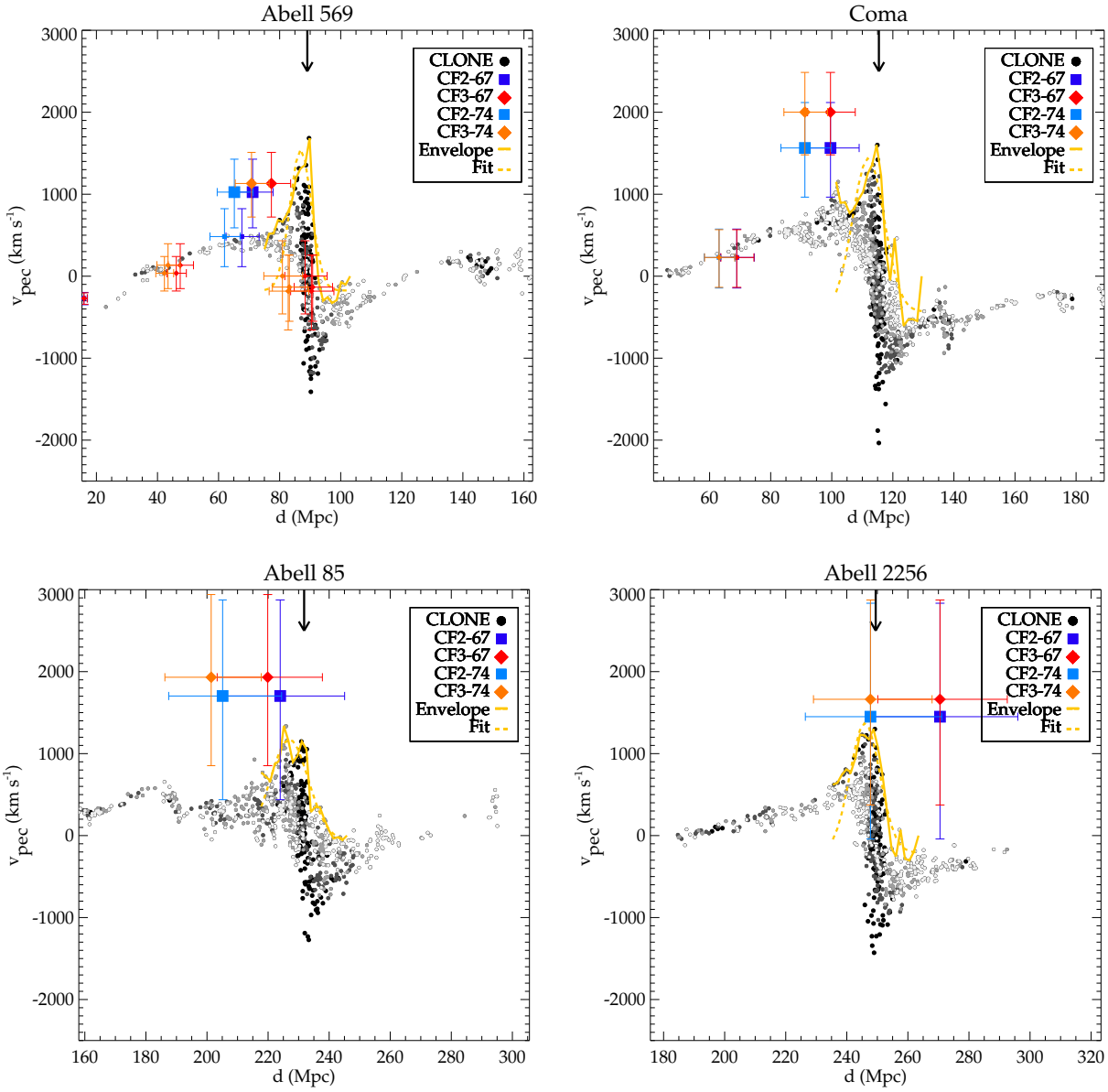

Fig. 4. Same as the bottom panels in Fig. 3 for four clusters at an increasing distance from us, from left to right, top to bottom. Although these clusters are less constrained, the agreement between observed and simulated waves is still visually good, especially for the first two. The dark matter halo masses in the simulation are $M = 9.0 \times 10^{14}\ M_\odot$, $M = 12.6 \times 10^{14}\ M_\odot$, $M = 6.6 \times 10^{14}\ M_\odot$, and $M = 11.7 \times 10^{14}\ M_\odot$ for Abell 569, Coma, Abell 85, and Abell 2256 cluster counterparts, respectively.

(see for instance Mohayaee & Tully 2005; Tully & Mohayaee 2004). This agreement is confirmed by observational data that follow the wave shape so as to reproduce its width. The next section expands on the link between wave properties and cluster masses. We note the adequacy between simulated and observed velocity wave shapes for Abell 569: small uncertainty peculiar velocities, not used to constrain this wave progenitor in the initial conditions' linear regime, follow the simulated wave contour. There are indeed two orange or red data points from the third catalog that have no blue counterpart in the second catalog. The 2D KS statistic small value confirms the adequacy.

Given their hosted galaxy peculiar velocity uncertainties, the lower mass limits of Coma, Abell 85, and Abell 2256 are reached. This was not fully expected, given that these clusters are at the edge of the constrained region (50%, 90%, and 99% of the constraints are in ∼75–80, 150–160, and 275–290 Mpc). Additional precise observational data are, however, required to probe the wave slopes and check their width to eventually tighten the constraint on the masses.

Figure 5 shows four additional velocity waves born from massive dark matter halos with which we can associate observed galaxies. The galaxies with the largest peculiar velocities are identified by their principal galaxy catalog (PGC) number at the top of each panel. Given the distance of these clusters and the sparsity and limit of our constraint catalog, there is an agreement. Tables 1 and 2 again confirm the visual impression. They also again highlight the limitations of both metrics. Both values must be given together to come to a conclusion about how much the observed and simulated lines of sight match. We identify other simulated velocity waves corresponding to local clusters (e.g. in the Perseus-Pisces region) but observational data is not of sufficient quality or absent in the infall region for comparisons. Nonetheless, all the halos and associated waves are used in the

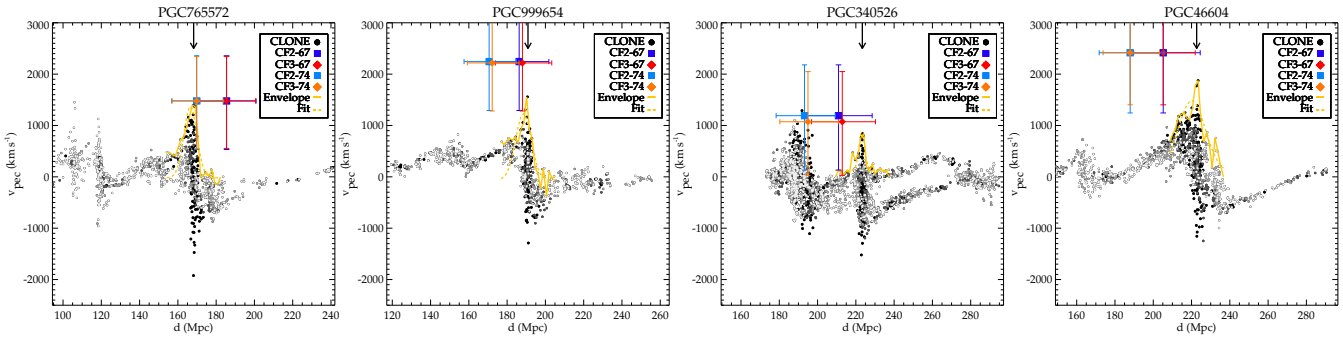

Fig. 5. Same as the bottom panels of Fig. 3 for four additional clusters. The names at the top of each panel are the PGC numbers of the galaxies with the highest velocity in the observational catalog at the given locations.

studies in the next section. The mass range is actually extended down to $2 \times 10^{14}\ M_{\odot}$.

4. Wave properties versus cluster masses

In the following, cluster and galaxy terminologies are used in place of the (massive) dark matter halo one.

4.1. Amplitude

The wave amplitude is the first obvious property to check against halo mass. Indeed, the deeper the gravitational potential well is, the faster galaxies should fall onto it. The amplitude is defined as the difference between the maximum and minimum peculiar velocities of galaxies falling onto the cluster, either from the front or from behind with respect to the synthetic observer. Figure 6 shows the amplitude of the simulated velocity waves as a function of the dark matter halo masses. Each filled black and red circle corresponds to a halo. Red ones stand for clusters identified in Figs. 3–5. While one immediately notices that there is a correlation between the wave amplitude and the halo mass, one can also point out that the amplitude is extremely difficult to measure in observational data and that there is a residual scatter. Indeed, measuring the amplitude in observational data implies getting accurate distance (peculiar velocity) estimates of galaxies exactly in the line of sight of the cluster with respect to us. It supposes first that there actually are galaxies that are exactly aligned. Then, identifying these galaxies and measuring their distances with high accuracy while they are falling onto the cluster from the front is already quite a challenge, let alone when they fall onto it from behind.

In any case, the residual scatter suggests that the amplitude alone, if it is measurable, cannot be used as a precise proxy for cluster mass estimates. Part of this scatter is probably due to the fact the galaxies are not perfectly aligned with us and the cluster. The gravitational potential well shape might also be responsible for another part of this scatter. To a lesser extent, the large-scale structure environment might also play a role.

4.2. Height

While the wave height was not expected to be a better proxy than the wave amplitude, it was interesting to check whether there was still a tight-enough correlation. Indeed, while it is challenging to have precise distance measurements for both galaxies falling from in front of and behind a cluster in the line of sight with respect to us, it might especially be feasible for galaxies falling from the front. The height is thus defined as the maximum

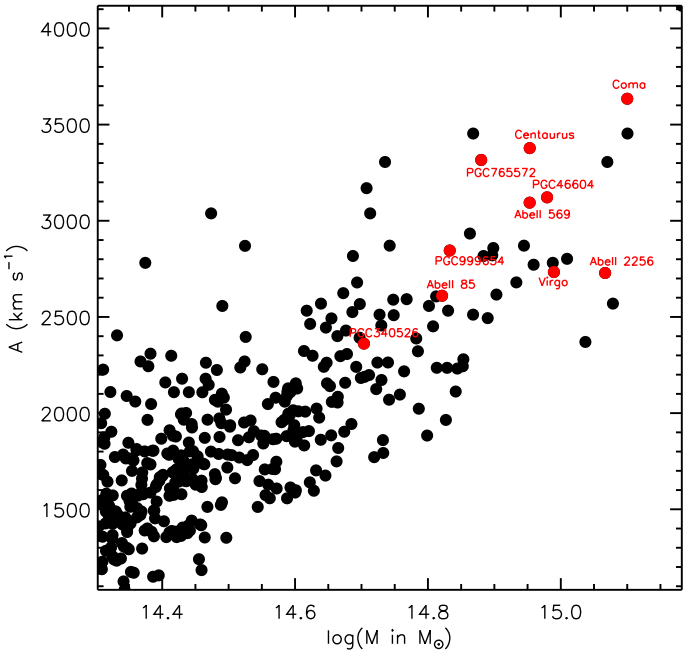

Fig. 6. Amplitude of the simulated velocity waves as a function of the dark matter halo masses. Amplitudes are obtained with dark matter halo minimum and maximum velocities. Halos shown in Figs. 3–5 are identified in red.

(minimum) peculiar velocities of galaxies falling onto the cluster from the front (behind) with respect to the synthetic observer. In Fig. 7, each black and red (blue and orange) filled circle stands for the height of a dark matter halo positive(negative)-half wave as a function of its mass. Heights are measured with velocities of galaxies falling from the front (behind) into the clusters. Red and orange are used for dark matter halos from Figs. 3 to 5.

A similar correlation to the amplitude is found, although with a somewhat larger scatter. Interestingly, it also shows that velocity waves are not symmetric: their maximum differs from their minimum. Both the potential well shape and the non-perfect alignment of the observer-galaxy-cluster or observer-cluster-galaxy might be the reason for this asymmetry. Nonetheless, because there still is a correlation and because in observational data it is easier to get accurate data points at the wave front than in its wake, it is legitimate to focus on the positive-half velocity wave shape to study more thoroughly the relation with the halo mass.

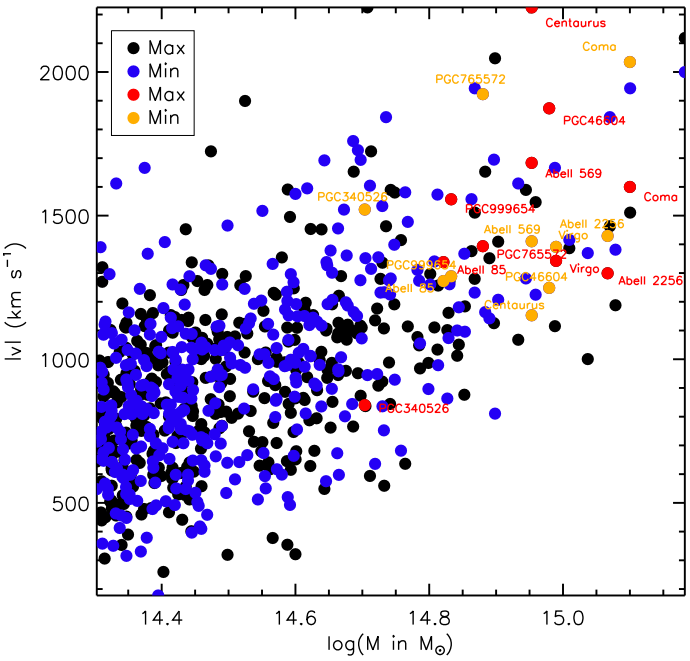

Fig. 7. Dark (blue) filled circles are heights of the simulated positive(negative)-half velocity waves as a function of the dark matter halo masses. Heights corresponds to maximum (minimum) dark matter halo velocities. Halos shown in Figs. 3–5 are identified in red (orange).

4.3. Height, width, and continuum

After deriving the positive-half wave envelope of every dark matter halo, as a proof of concept we chose to fit the simplest model possible, a Gaussian-plus-continuum model, to each one of them as follows:

$$v_{\rm pec} = A_{\rm fit} \times e^{\frac{-(d-d_0)^2}{2\sigma_{\rm fit}^2}} + C_{\rm fit}, \quad (5)$$

where $A_{\rm fit}$, $\sigma_{\rm fit}$, and $C_{\rm fit}$ are, respectively, the Gaussian amplitude, its standard deviation, and a continuum. d_0 depends on the halo distance and has no other purpose than centring the Gaussian on zero. Its sole physical meaning is to be the actual distance of the halo. The amplitude is related to the positive-half wave envelope height, while the standard deviation is linked to its width. Finally, the continuum gives the positive-half wave offset from a zero average velocity. For visualisation, envelopes and their fits for halos presented in Figs. 3–5 are shown as solid and dashed lines in these same figures. In observational catalogs, velocity waves are more likely to be highlighted with only a few galaxies. Degrading the information in the simulation by using only velocity-wave envelopes and their fits is, thus, coherent with the information available in observational catalogs for further applications to observations.

Figure 8 gathers the three parameters of the fits and halo masses for a concomitant study to highlight an eventual multi-parameter correlation. The Gaussian amplitude is represented as a function of the Gaussian standard deviation while the colour scale stands for the continuum. From black and violet to red, the continuum decreases from positive values to negative ones. The model uncertainty is shown as error bars for the amplitude and standard deviation. The colour scale smoothness includes the continuum uncertainty. The Gaussian-plus-continuum model choice proves to be robust, given the tiny error bars that it results in. The filled circle sizes are proportional to the dark matter halo masses. Finally, an additional small filled red circle is used to identify each halo analyzed in Figs. 3–5.

The previous subsection (Sect. 4.2) showed that there is a correlation between the wave height and the halo mass. It is thus not surprising to find that the more massive the halo is (larger circle), the larger the Gaussian amplitude is (larger value). The histograms in the top panel confirm that the median amplitude increases with the bin of mass (dashed lines from dark grey to light grey). As was stated above, the Gaussian amplitude is the counterpart of the positive-half wave height.

In addition, there is a small correlation between the amplitude and standard deviation, and thus the halo mass. More massive halos seem to give birth to wider waves on average. The histograms in the right panel confirm that the median standard deviation increases with the bin of mass (dashed lines from dark grey to light grey). The scatter however increases with the decrease in mass, as is shown by the dashed contours in the middle panel. These contours delimit the amplitude-standard deviation region containing 95% of the clusters of a given mass bin. It highlights the standard deviation dependency on the halo triaxiality, and thus on its orientation with respect to us, and to the environment especially for the halos of the lowest mass bin. A similar conclusion is valid for the continuum: the smaller the continuum, except for the extreme values, is, the more massive the halo is on average. The scatter is also quite large in that case. A correlation between the standard deviation value and that of the continuum is noticeable, especially for the low mass bin. A strong dependence on the global environment of the dark matter halo, in addition to the halo mass, might also be a cause here.

Interestingly, a general pattern emerges:
– The most massive halos ($\gtrsim 5 \times 10^{14}\,M_\odot$) tend to give birth to positive-half waves that have a positive or slightly negative continuum in addition to high amplitude and standard deviation values (the two lighter grey colours).
– The less massive halos ($2 \times 10^{14}\,M_\odot \lesssim M \lesssim 3 \times 10^{14}\,M_\odot$) tend to give birth to positive-half waves that have a low amplitude, a highly scattered but correlated continuum, and standard deviation values (darker grey colour).
– Intermediate mass halos ($3 \times 10^{14}\,M_\odot \lesssim M \lesssim 5 \times 10^{14}\,M_\odot$) give rise to positive-half waves that have intermediate amplitude values and on average higher continuum values. Such values permit distinguishing them from the most massive halos, with which they can share high amplitude and possibly standard deviation values (intermediate grey colour).

It is probable that the global environment or cosmic web is responsible for such a finding. We will investigate this link in more detail in future studies.

Halos are also segregated in different continuum value classes. There seems to be a different correlation for each continuum value class:
– Halos with fits resulting in a high (close to zero) continuum value seem to have masses correlated with the Gaussian amplitudes but not so much with the Gaussian standard deviations that appear to have low values (present a large scatter).
– Halos with fits resulting in a very low continuum value have both amplitudes and standard deviations correlated together as well as with the masses.
– Halos with fits resulting in either positive or negative intermediate continuum values present masses correlated with amplitudes and to a lesser extent with standard deviations.

To summarise, since the fit parameters are interdependent, a global fit to the velocity wave seems the best approach to

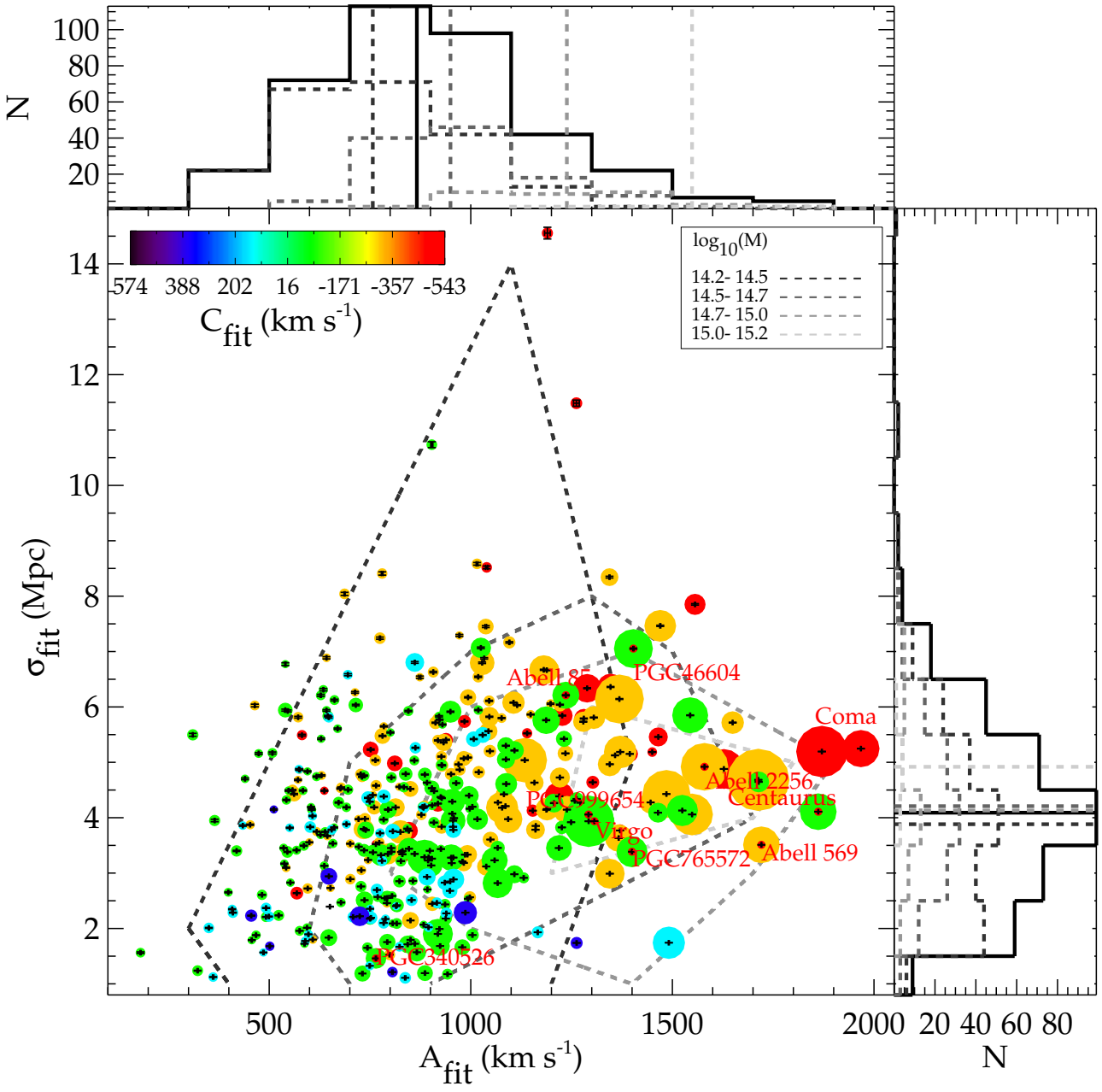

Fig. 8. Parameters of the Gaussian-plus-continuum fit to the simulated positive-half velocity waves. $\sigma_{\rm fit}$ stands for the Gaussian standard deviation, $A_{\rm fit}$ for its amplitude, and $C_{\rm fit}$ for the continuum. The filled circle sizes are proportional to dark matter halo masses. Tiny error bars on the standard deviation and amplitude resulting from fitting the envelopes highlight the adequacy of the model choice. Halos shown in Figs. 3–5 are identified with red name tags and additional small filled red circles. The dashed grey lines stand for the surfaces that encompass 95% of the halos of a given mass bin. The mass bin increases from dark to light grey. Histograms of the amplitude and standard deviation values for the full sample of halos (solid black line) and per bin of mass (dashed grey lines) are given in the top and right panels, respectively, together with medians. The more massive the halos are the larger the amplitude is, and to a lesser extent the standard deviation is, on average. The scatter in the standard deviation values increases with the decrease in mass, probably because the environment plays a more important role for the halos of the smallest mass bin, while massive halos are more active in shaping their environment.

obtain cluster rough mass estimates rather than single and independent measurements of amplitude, height, and width. Because different categories appear among halos, in future studies a machine learning approach might become handy to actually get accurate-enough mass estimates from sparse observations. In a first approach, the simple Gaussian-plus-continuum fit presented here could be used as summary statistics. Meanwhile, in the next subsection, we propose another single value summary statistics: the centred ζ metric.

4.4. Centred ζ metric

The ζ metric might be a good proxy for estimating cluster mass, as the wave shape is related to the cluster mass. Since it measures the adequacy between observational data points and simulated waves, it could assign the best-fitted wave type, and thus mass, to an observational data point set. However, the ζ metric depends on the distance to the cluster. It can thus only be applied to observed clusters and their simulated replicas. To remove this

dependence, the centred ζ metric, or ζ_c metric, was introduced:

$$\zeta_c = \frac{1}{n}\sum_{i=1}^{n} \min\{\sqrt{[v_{\rm obs}[i] - v_{\rm sim}]^2 + [(d_{\rm obs}[i] - \tilde{d}_{\rm sim}) \times H_0]^2}\}, \tag{6}$$

where n is still the number of observed galaxies in the line of sight. v_X are again the galaxy or subhalo observed and simulated peculiar velocities and d_X are their distances. However, the distances of the simulated subhalos, $d_{\rm sim}$, are shifted so that the simulated and observed clusters' centres match, $\tilde{d}_{\rm sim}$.

In the previous sections, four simulated and observed clusters were matched using more than one observational data point that passed the small uncertainty threshold. These clusters are Virgo, Centaurus, Abell 569, and Coma. The position of other halos were re-centred to appear at the same distance as the replicas. Figures 9 and 10 show the lines of sight, waves included, for the re-centred halos closest in mass to the different replicas. Observational data points corresponding to the replicas' counterparts are overplotted. The top left panels show the lines of sight of the replicas. The other panels highlight those of the other halos; that is, those sharing similar masses but different environments and histories. Overall, the lines of sight hosting halos of similar masses appear to be in agreement with the observational data points that they have been assigned to. This adequacy reinforces the existence of a strong link between velocity waves and cluster masses.

ζ_c values were derived by comparing the observed and simulated data points. In Fig. 11, these values, their means, and standard deviations are represented as filled black circles and error bars per bin of mass for the four clusters. First, the ζ values for the replicas, given by filled red circles, are on average on the low side compared to the ζ_c values. Second, the scatter and mean of the ζ_c values vary with the bin and with the compared observed and simulated lines of sight. The smallest mean and scatter are obtained for masses similar to the replica: the filled red circles are at best in the bin of mass with the smallest mean or scatter of ζ_c values, and at worst in that just next to it. Using twice the current mass bin size gives comparable results but larger uncertainties on the mass estimates. Using half the current mass bin size also results in similar values but tends to favour the bin just above that which includes the ζ value. We, thus, stuck to our current bin size. The ζ_c values suggest that they might collectively be good proxies for mass estimates. Providing enough simulated halos, deriving the mean and scatter of ζ_c values per bin of mass associated with these halos and an observational dataset, permits an estimation of the mass of the cluster responsible for the wave in the observational data. It adds weight to the idea that machine learning techniques could be used to learn about this relation between wave and mass and provide cluster mass estimates. This will be investigated in future work.

Table 3 gathers the observational virial mass estimates from Tully (2015) for the four clusters, as well as those of their replicas in the CLONE. The last column gives the mass bin that corresponds to the ζ_c values with the smallest mean and scatter. The mass estimates are in good agreement, except for Abell 569. The observational mass estimate is one order of magnitude below the ζ_c-metric estimate and the mass of the simulated replica. However, Abell 569 consists of two separated concentrations separated by ∼1.5 Mpc (Focardi et al. 1984). Given the resolution at which the CLONE initial conditions were constrained, two concentrations might be replaced with one larger halo. Moreover, the wave signals of two close-by simulated and observed clusters can become entangled, affecting their mass estimates. This highlights a limit of the ζ_c metric. Clusters need to be sufficiently far apart for their waves to be distinguishable.

5. Conclusions

Galaxy clusters are good cosmological probes, provided their mass estimates are accurately determined. Fueled with large imaging surveys, stacked weak lensing is the most promising mass estimate method, though it provides estimates within relatively small radii. Given the large amount of accompanying redshift and spectroscopic data overlapping the imaging surveys, we must take the opportunity to also calibrate with reasonable accuracy a method based on galaxy dynamics. Two independent measures indeed hold better constraints on the cosmological model. The infall zones of galaxy clusters are probably less sensitive to baryonic physics, and thus mostly shielded from challenging systematics, and they probe large radii. These manifestations of a tug of war between gravity and dark energy provide a unique avenue to test modified gravity theories when comparing the resulting mass estimates to those from stacked weak lensing measurements. Combined with stacked weak lensing results, they might even yield evidence that a departure from general relativity on cosmological scales is responsible for the expansion acceleration.

The accurate calibration of the relation between infall zones' properties and cluster masses starts with careful comparisons between cosmological simulations and observations. In this paper, we thus present the largest and highest-resolution CLONE simulation that we have built so far to numerically reproduce our cosmic environment. This simulation stems from initial conditions constrained by the peculiar velocities of local galaxies. By introducing this cosmological dark matter CLONE of the local large-scale structure with a particle mass of $\sim 10^9\,M_\odot$ within a ∼738 Mpc box, we have generated sufficient resolution to study the effect of the gravitational potential of massive local halos on the velocity of (sub)halos. We can also make comparisons with the effect produced by their observational cluster counterparts.

Velocity waves stand out in radial peculiar velocity (see the diagram of the distance to a box-centred synthetic observer). Lines of sight that include velocity waves caused by the most massive dark matter halos of the CLONE simulation and those born from their observed local cluster counterparts are in agreement, especially the clusters the closest to us that are the best constrained (e.g. Virgo and Centaurus). Secondary waves due to smaller groups in (quasi) the same line of sight as the most massive clusters stand out equally even though they are further into the non-linear regime. Indeed, prior to full non-linear evolution to the $z = 0$ state, assuming ΛCDM, CLONE initial conditions are constrained solely with the linear theory, a power spectrum, and highly uncertain and sparse local peculiar velocities. The visual matching between simulated and observed lines of sight is confirmed with 2D KS statistic values and tests as well as with our own ζ metric. Contrary to the 2D KS statistic, the ζ metric takes into account the real distance of galaxies along the entire lines of sight (not only the studied fractions). The ζ metric is however more sensitive to the fact that observational uncertainties are not taken into account in these metrics. The two metrics appear to be complementary. They show that the closest clusters have the best reproduced lines of sight. The lines of sight of clusters at the edges of the constrained region and even slightly beyond are reproduced by the simulation to a smaller extent (a lower mass limit is reached).

Additionally, a Gaussian-plus-continuum fit to the envelope of the positive-half of all the velocity waves born from dark

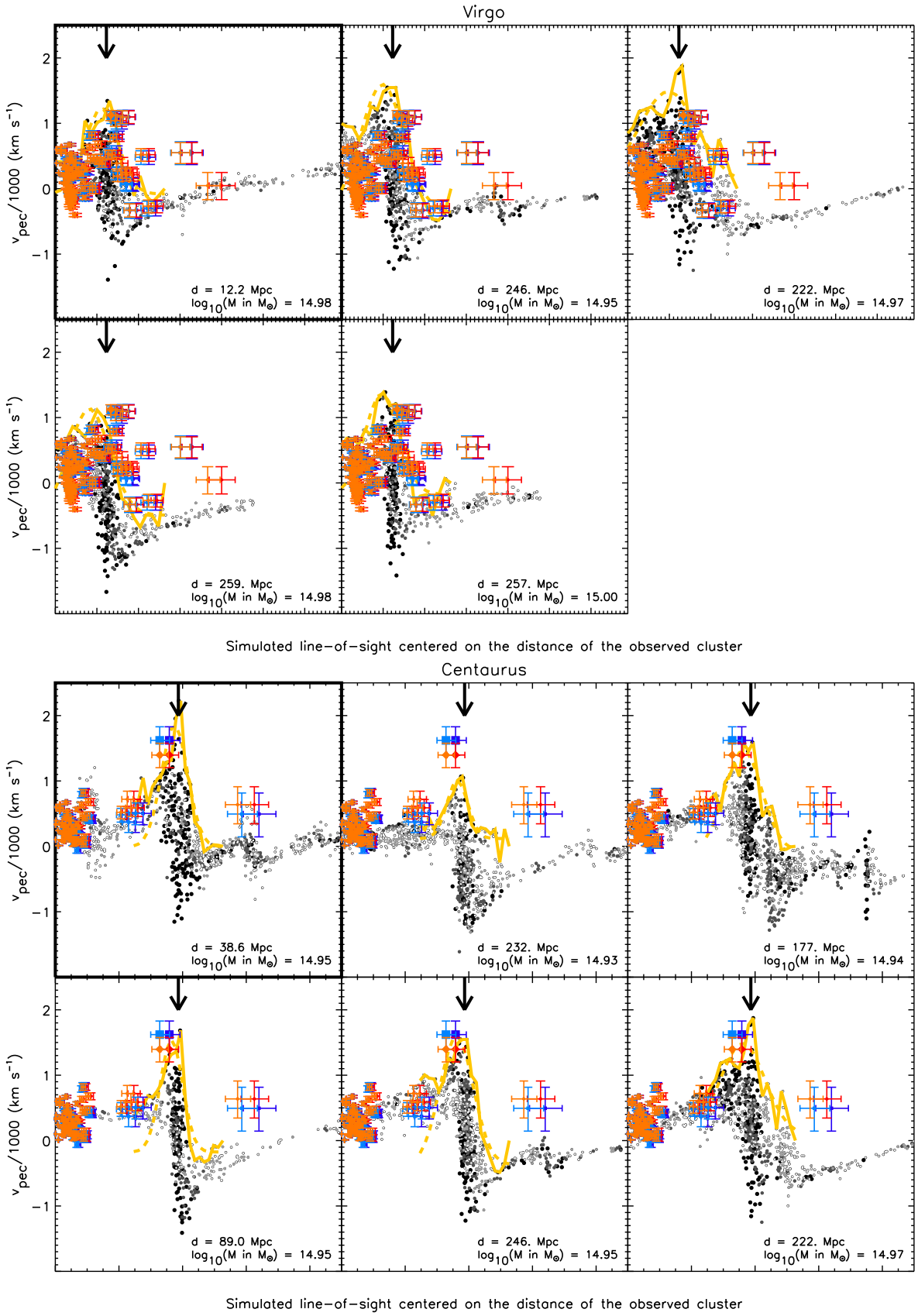

Fig. 9. Same as the bottom panels in Fig. 3, with additional comparisons with other halos sharing similar masses but different environments and histories. The first panel of each subfigure stands for the line of sight that includes the replica of the observed cluster whose name is given at the top of the panel. The other panels show the lines of sight that include halos with very similar masses to the replicas. They have been shifted, though, to be located at the same distance as the simulated replicas, in order to be able to overplot observational data points. Their original distance to the observer in the simulation is given together with their mass in each panel.

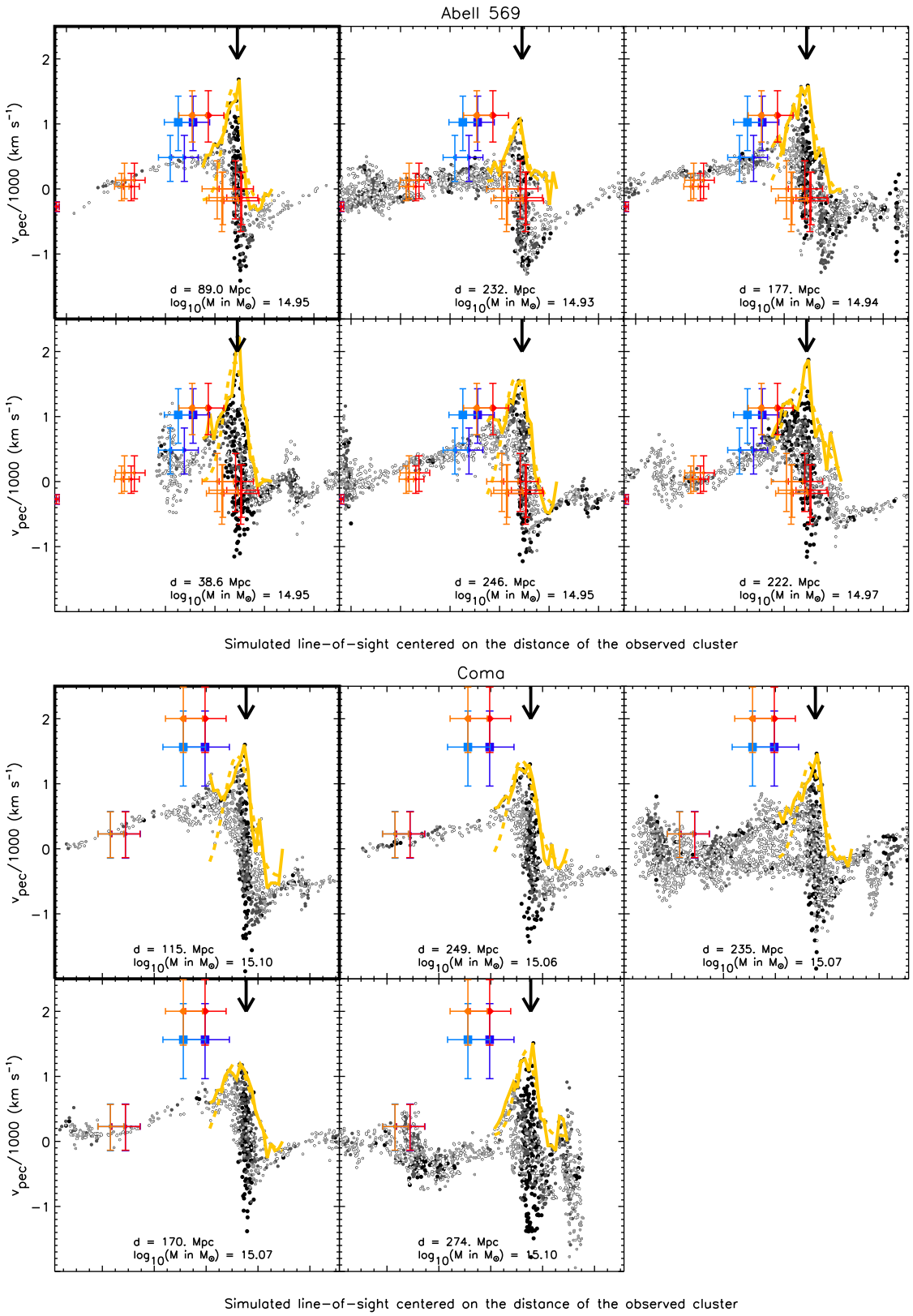

Fig. 10. Same as Fig. 9 but for the Abell 569 and Coma clusters.

matter halos more massive than $2 \times 10^{14}\,M_{\odot}$ in the simulation reveals both the variety and complexity of the potential wells as well as the correlation of the fit parameters with the halo masses. Overall, the Gaussian amplitude is mostly linked to the halo mass – but for a few exceptions – with a residual scatter. Although the Gaussian standard deviation is not always correlated with the mass, it can be slightly correlated with the Gaussian amplitude, and thus with the mass. The continuum is certainly an interesting parameter to consider as it permits splitting the halos into different classes. Each continuum

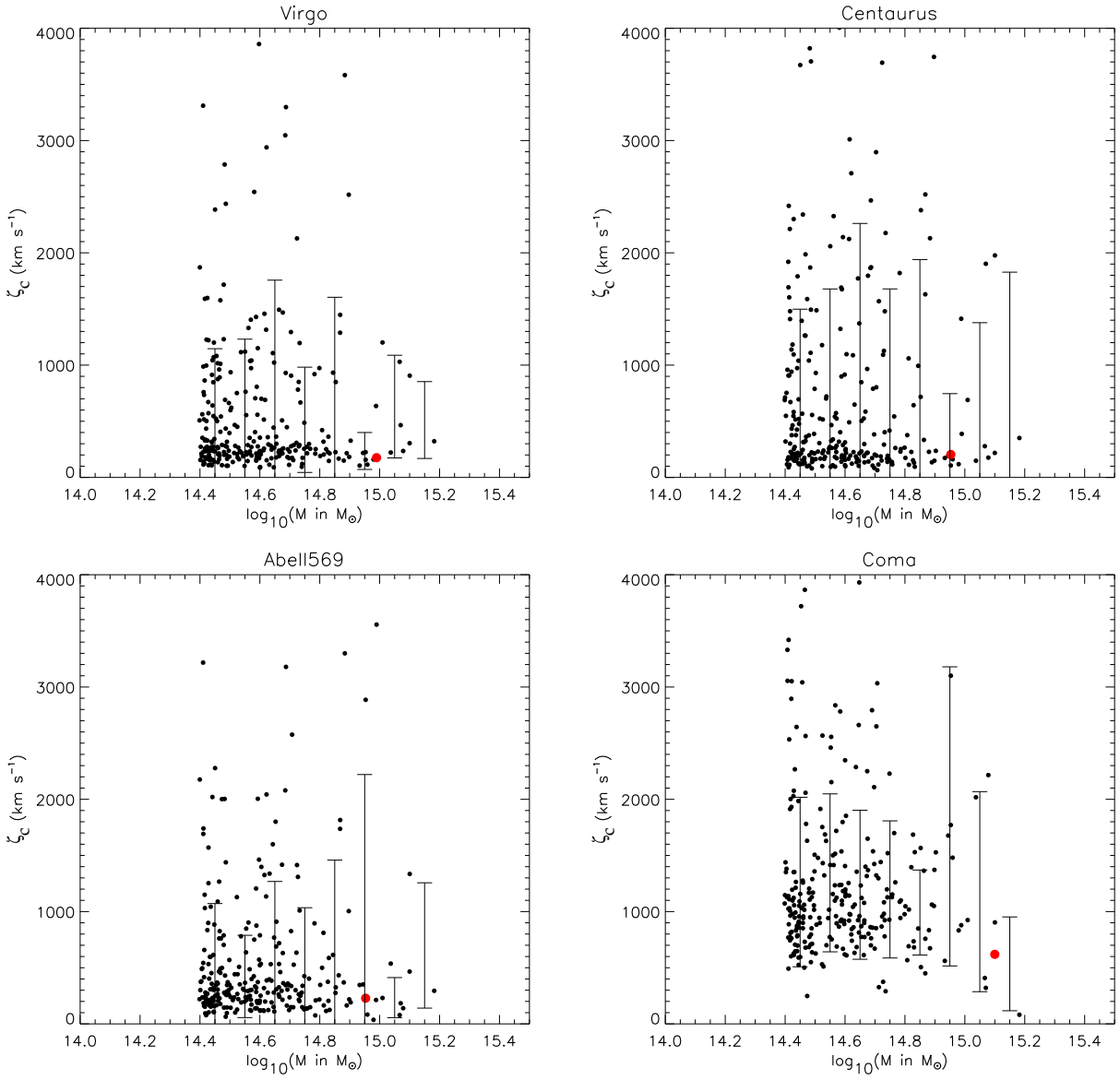

Fig. 11. Centred ζ-metric, or ζ_c-metric, values in km s^{-1} as a function of the halo mass. It measures the difference between the simulated and observed lines of sight that include the halos or clusters. Halos that are replicas of the observed clusters, named at the top of each panel, serve as a reference for the shift in the distance of the other halos. The filled red circles give the ζ metric value obtained for the replicas. The higher ζ_c is, the more different the lines of sight are.

value seems to drive a given correlation between the Gaussian amplitude and the halo mass and, to a smaller extent, with the Gaussian standard deviation. To summarise, parameter fits are completely interdependent, and therefore a global fit to the velocity wave is the best approach to obtain a first rough cluster mass estimate.

We further derived centred ζ-metric or ζ_c-metric values for observed and simulated lines of sight including different mass galaxy clusters. Simulated halos were shifted in distance to match those of the observed clusters (hence the term 'centred' ζ metric). The ζ_c values per bin of mass present a minimum mean and variance in agreement with the ζ value obtained when comparing simulated and observed lines of sight of the cluster and its replica. This suggests that the ζ_c metric can provide the mass range estimate of a cluster given an observational dataset that includes its wave and several simulated cluster re-centred lines of sight. It also bolsters the idea that machine learning techniques should be able to learn wave-type and associated masses to finally give cluster mass estimates. We will investigate this in future work.

First and foremost, this work confirms the potential of the velocity wave technique to get massive cluster mass estimates and test gravity and cosmological models. Our CLONE simulation, with the first shown reproduction of observed lines of sight including velocity waves, could in the near future provide the zero point of galaxy infall kinematic technique calibrations (Zu & Weinberg 2013). A Bayesian inference model embedding a machine learning technique built and trained on random simulated galaxy surveys that is then applied to both constrained simulated and observed galaxy surveys must recover the same local velocity waves and corresponding mass estimates to be validated. Our CLONE simulation will moreover allow observational biases to be minimised, as any real environmental and cluster property will be reproduced for one-to-one comparisons. Local kinematic mass estimates can then become accurate. Once compared with other techniques of local galaxy cluster mass

Table 3. Cluster mass estimates from observations (Tully 2015), from the replica and using the ζ_c metric to compare observed and several simulated lines of sight.

Cluster	Observation	CLONE-Replica in $10^{14}\,M_\odot$	ζ_c metric
Virgo	7.01	9.8	[7.9–10]
Centaurus	10.8	9.0	[7.9–10]
Abell 569	0.67	9.0	[10–13]
Coma	15.9	12.6	[13–16]

estimates, they will permit the calibration of the zero-point of these other techniques to be applied to further and further away clusters.

Acknowledgements. The authors would like to thank the referee for their comments that help improve the quality of this manuscript. The authors acknowledge the Gauss Centre for Supercomputing e.V. (www.gauss-centre.eu) and GENCI (https://www.genci.fr/) for funding this project by providing computing time on the GCS Supercomputer SuperMUC-NG at Leibniz Supercomputing Centre (www.lrz.de) and Joliot-Curie at TGCC (http://www-hpc.cea.fr), grants ID: 22307/22736 and A0080411510 respectively. This work was supported by the grant agreements ANR-21-CE31-0019 / 490702358 from the French Agence Nationale de la Recherche/DFG for the LOCALIZATION project and ERC-2015-AdG 695561 from the European Research Council (ERC) under the European Union's Horizon 2020 research and innovation program for the ByoPiC project (https://byopic.eu). This work was supported by the Programme National Cosmologie et Galaxies (PNCG) of CNRS/INSU with INP and IN2P3, co-funded by CEA and CNES. KD acknowledges support by the COMPLEX project from the ERC under the European Union's Horizon 2020 research and innovation program grant agreement ERC-2019-AdG 882679. The authors thank the referee for their comments. JS thanks Marian Douspis for useful comments, the ByoPiC team, the IAP 'Origin and evolution of galaxies' team and her CLUES collaborators for discussions. NM acknowledges funding by the European Union through a Marie Skłodowska-Curie Action Postdoctoral Fellowship (Grant Agreement: 101061448, project: MEMORY).

References

Aubert, D., Pichon, C., & Colombi, S. 2004, MNRAS, 352, 376
Burke, D. 2006, Amer. Phys. Soc., APS Meeting, 17.004
Carlberg, R. G., Yee, H. K. C., Ellingson, E., et al. 1997, ApJ, 485, L13
Cirasuolo, M., Afonso, J., Carollo, M., et al. 2014, in Ground-based and Airborne Instrumentation for Astronomy V, eds. S. K. Ramsay, I. S. McLean, & H. Takami, SPIE Conf. Ser., 9147, 91470N
Davis, T. M., & Scrimgeour, M. I. 2014, MNRAS, 442, 1117
de Jong, R. S., Bellido-Tirado, O., Chiappini, C., et al. 2012, in Ground-based and Airborne Instrumentation for Astronomy IV, eds. I. S. McLean, S. K. Ramsay, & H. Takami, 84460T, SPIE Conf. Ser., 8446
Diaferio, A. 1999, MNRAS, 309, 610
Dolag, K., Sorce, J. G., Pilipenko, S., et al. 2023, A&A, 677, A169
Fasano, G., & Franceschini, A. 1987, MNRAS, 225, 155
Focardi, P., Marano, B., & Vettolani, G. 1984, A&A, 136, 178
Gottlöber, S., Hoffman, Y., & Yepes, G. 2010, arXiv e-prints [arXiv:1005.2687]
Green, J., Schechter, P., Baltay, C., et al. 2012, arXiv e-prints [arXiv:1208.4012]
Heisler, J., Tremaine, S., & Bahcall, J. N. 1985, ApJ, 298, 8
Hernández-Martínez, E., Dolag, K., Seidel, B., et al. 2024, A&A, in press, https://doi.org/10.1051/0004-6361/202449460
Huchra, J. P., Macri, L. M., Masters, K. L., et al. 2012, ApJS, 199, 26
Jasche, J., & Wandelt, B. D. 2013, MNRAS, 432, 894
Karachentsev, I. D., & Nasonova, O. G. 2013, MNRAS, 429, 2677
Karachentsev, I. D., Nasonova, O. G., & Courtois, H. M. 2013, MNRAS, 429, 2264
Kitaura, F.-S. 2013, MNRAS, 429, L84
Kravtsov, A. V., & Borgani, S. 2012, ARA&A, 50, 353
Lebeau, T., Ettori, S., Aghanim, N., & Sorce, J. G. 2024a, A&A, in press, https://doi.org/10.1051/0004-6361/202450146
Lebeau, T., Sorce, J. G., Aghanim, N., Hernández-Martínez, E., & Dolag, K. 2024b, A&A, 682, A157
Malavasi, N., Sorce, J. G., Dolag, K., & Aghanim, N. 2023, A&A, 675, A76
Mamon, G. A., Biviano, A., & Murante, G. 2010, A&A, 520, A30
Mandelbaum, R., Seljak, U., Cool, R. J., et al. 2006, MNRAS, 372, 758
McAlpine, S., Helly, J. C., Schaller, M., et al. 2022, MNRAS, 512, 5823
Mohayaee, R., & Tully, R. B. 2005, ApJ, 635, L113
Olchanski, M., & Sorce, J. G. 2018, A&A, 614, A102
Peacock, J. 2008, A Decade of Dark Energy: Spring Symposium, eds. N. Pirzkal & H. Ferguson, www.stsci.edu/institute/conference/spring2008, 33
Peacock, J. A. 1983, MNRAS, 202, 615
Peirani, S. 2010, MNRAS, 407, 1487
Peirani, S., & de Freitas Pacheco, J. A. 2006, Nat. Astron., 11, 325
Planck Collaboration XVI. 2014, A&A, 571, A16
Planck Collaboration XXIV. 2016, A&A, 594, A24
Pratt, G. W., Arnaud, M., Biviano, A., et al. 2019, Space Sci. Rev., 215, 25
Sanchis, T., Mamon, G. A., Salvador-Solé, E., & Solanes, J. M. 2004, A&A, 418, 393
Sorce, J. G. 2015, MNRAS, 450, 2644
Sorce, J. G. 2018, MNRAS, 478, 5199
Sorce, J. G., & Tempel, E. 2017, MNRAS, 469, 2859
Sorce, J. G., & Tempel, E. 2018, MNRAS, 476, 4362
Sorce, J. G., Gottlöber, S., Hoffman, Y., & Yepes, G. 2016a, MNRAS, 460, 2015
Sorce, J. G., Gottlöber, S., Yepes, G., et al. 2016b, MNRAS, 455, 2078
Sorce, J. G., Hoffman, Y., & Gottlöber, S. 2017, MNRAS, 468, 1812
Sorce, J. G., Blaizot, J., & Dubois, Y. 2019, MNRAS, 486, 3951
Sorce, J. G., Dubois, Y., Blaizot, J., et al. 2021, MNRAS, 504, 2998
Tempel, E., Kruuse, M., Kipper, R., et al. 2018, A&A, 618, A81
Teyssier, R. 2002, A&A, 385, 337
Tonry, J. L., & Davis, M. 1981, ApJ, 246, 680
Tully, R. B. 2015, AJ, 149, 54
Tully, R. B., & Mohayaee, R. 2004, in IAU Colloq. 195: Outskirts of Galaxy Clusters: Intense Life in the Suburbs, ed. A. Diaferio, 205
Tully, R. B., & Shaya, E. J. 1984, ApJ, 281, 31
Tully, R. B., Courtois, H. M., Dolphin, A. E., et al. 2013, AJ, 146, 86
Tully, R. B., Courtois, H. M., & Sorce, J. G. 2016, AJ, 152, 50
Tweed, D., Devriendt, J., Blaizot, J., Colombi, S., & Slyz, A. 2009, A&A, 506, 647
Weinberg, S. 1972, Gravitation and Cosmology: Principles and Applications of the General Theory of Relativity (Wiley-VCH)
Weinberg, D. H., Mortonson, M. J., Eisenstein, D. J., et al. 2013, Phys. Rep., 530, 87
Zu, Y., & Weinberg, D. H. 2013, MNRAS, 431, 3319
Zu, Y., Weinberg, D. H., Jennings, E., Li, B., & Wyman, M. 2014, MNRAS, 445, 1885

Appendix A: Comparisons with SIBELIUS-DARK

Table A.1. KS statistic (first two lines) and ζ metric in km s^{-1} (last two lines), like in Tables 1 and 2 but for SIBELIUS-DARK clusters.

Cluster	SIBELIUS/CF2		SIBELIUS/CF3		Random/CF3
Cylinder radius	10 Mpc	2.5 Mpc	10 Mpc	2.5 Mpc	2.5 Mpc
Virgo	0.80	0.88	0.77	0.87	/
Centaurus	0.85	0.90	0.91	0.88	/
Virgo	129	208	116	207	11200
Centaurus	171	312	181	279	11365

Table A.2. Cluster mass estimates from observations (Tully 2015), the SIBELIUS-replica, and the ζ_c metric. SIBELIUS-DARK mass estimates are M_{200}. They are ∼1.3 times smaller than M_{vir} (Sorce et al. 2016a) .

Cluster	Observation	SIBELIUS-Replica in 10^{14} $M_\odot$	ζ_c metric
Virgo	7.01	3.5	[7.9-10]
Centaurus	10.8	4.5	[13-16]

This appendix compares the observed lines of sight to those simulated in the SIBELIUS-DARK constrained simulations (McAlpine et al. 2022). Contrary to CLONE, this simulation is constrained with a complete (to a given limit) observational redshift survey. Given the halos identified in McAlpine et al. (2022) and the observational dataset with the required uncertainty threshold available to make a comparison, three clusters were selected: Virgo, Centaurus, and Coma. The SIBELIUS-DARK and observed lines of sight are shown in Figure A.1. The lines of sight are in good agreement with the observational data points except for Coma-SIBELIUS. However, a smaller group in front of Coma-SIBELIUS matches some observational data points. Because of this mismatch with the main cluster wave, Coma was removed from further comparisons.

Tables A.1 gather the KS-statistic and ζ-metric values. The two clusters' lines of sight seem to be reproduced in a comparable way in CLONE and SIBELIUS, with a tiny advantage for Virgo-CLONE (Virgo-SIBELIUS) when using the KS statistic (ζ metric). However, the SIBELIUS-DARK line of sight has twice as many simulated data points to compare to a comparable number of observational data points, or fewer, than for CLONE's line of sight. This highlights a limitation of the ζ metric, which favours simulated lines of sight with a larger number of simulated data points to match with a smaller number of observed data points. There are indeed more choices. This results in a higher probability of finding a smaller minimum.This difference is partly due to the semi-analytical model used in SIBELIUS-DARK. Although we restricted this sample in mass to match our dark matter subhalo list, the samples are not strictly identical. In addition, replicas are not located exactly at the same positions in CLONE versus SIBELIUS-DARK, implying slightly different matched lines of sight with observations. Synthetic line-of-sight replicas are not shifted to match the observed lines of sight but simply overplotted.

In Table A.2, the ζ_c metric provides an estimate of the mass of the clusters given that the lines of sight match the SIBELIUS-DARK ones. While for Virgo the mass range is the same as for CLONE, it is higher for Centaurus. The mix between two waves in the Centaurus-SIBELIUS line of sight might be the cause. The ζ_c metric is potentially biased to be high when two halo signatures are entangled, as is shown for Abell 569-CLONE.

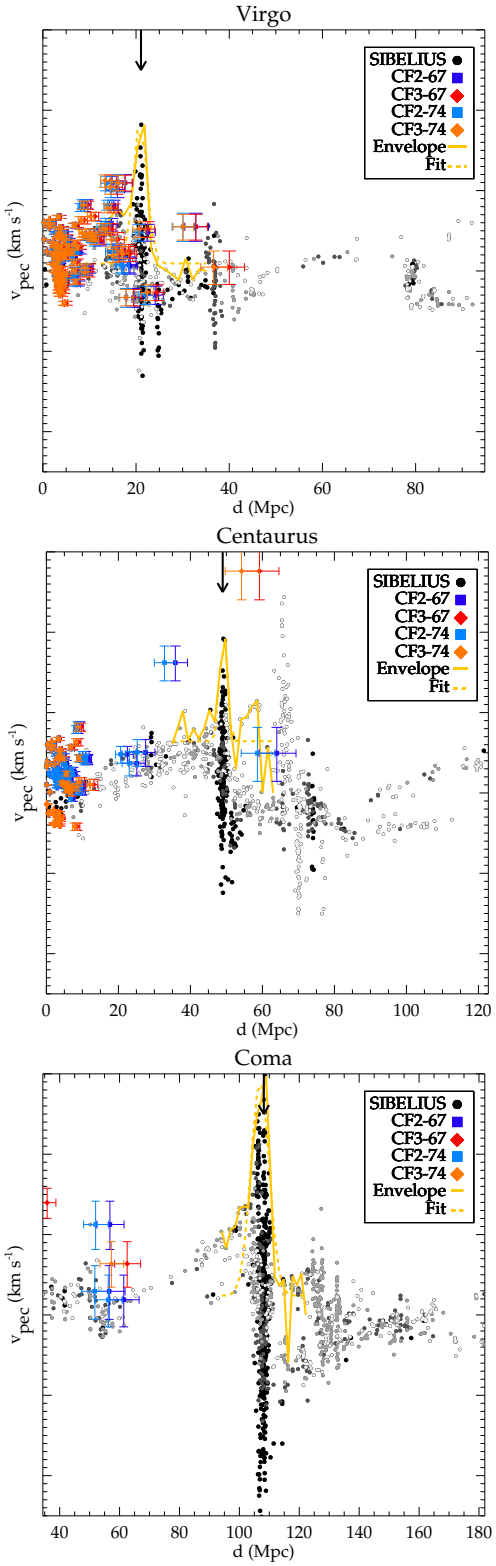

Fig. A.1. Same as Figure 3 but for the SIBELIUS-DARK clusters (McAlpine et al. 2022).